NEUROSCIENCE

Single metal-organic framework–embedded nanopit arrays: A new way to control neural stem cell differentiation

Yeon-Woo Cho[1]†, Seohyeon Jee[2]†, Intan Rosalina Suhito[1], Jeong-Hyeon Lee[1], Chun Gwon Park[3,4], Kyung Min Choi[2,5]*, Tae-Hyung Kim[1]*

Stable and continuous supply of essential biomolecules is critical to mimic in vivo microenvironments wherein spontaneous generation of various cell types occurs. Here, we report a new platform that enables highly efficient neuronal cell generation of neural stem cells using single metal-organic framework (MOF) nanoparticle–embedded nanopit arrays (SMENA). By optimizing the physical parameters of homogeneous periodic nanopatterns, each nanopit can confine single nMOFs (UiO-67) that are specifically designed for long-term storage and release of retinoic acid (RA). The SMENA platform successfully inhibited physical interaction with cells, which contributed to remarkable stability of the nMOF (RA⊂UiO-67) structure without inducing nanoparticle-mediated toxicity issues. Owing to the continuous and long-term supply of RA, the neural stem cells showed enhanced mRNA expressions of various neurogenesis-related activities. The developed SMENA platform can be applied to other stem cell sources and differentiation lineages and is therefore useful for various stem cell–based regenerative therapies.

INTRODUCTION

In developmental processes, various cells are generated from stem cells wherein their behaviors are strictly and intimately controlled by several key factors, including cell-cell interactions, cell-environment interactions, and concentration gradient in vital nutrients/proteins (1–4). However, unlike the in vivo environment, owing to the absence of extrinsic supports from surrounding cells and extracellular matrix components, guiding stem cell fates ex vivo is generally initiated and proceeded by the addition of various predefined factors (5–9). In this case, concentrated major differentiation molecules/proteins were added to the medium and kept for 2 to 3 days. However, upon medium treatments, the cells experienced chemically induced stress due to the high concentration of biomolecules and proteins at the initial stage, for example, ascorbic acid, retinoic acid (RA), and fibroblast growth factor/brain-derived neurotrophic factor for neurogenesis (10–14). Those differentiation factors are consumed by cells during the differentiation process, which results in their shortage of supply after 24 to 48 hours of incubation. This fluctuation in the concentrations of key factors within the whole differentiation period is completely different from in vivo developmental and differentiation processes and ultimately negatively affects the guiding efficiency of the stem cell fates (15–18). Therefore, a new type of platform that enables long-term and stable release or supply of key differentiation factors to target cells is highly needed.

Metal-organic frameworks (MOFs), compounds constructed with metal ions and organic ligands, have emerged as a promising porous material due to the outstanding uniformity in their crystalline structure and variability in various factors, including structure type, organic functionality, geometry, size of metal-containing unit, size of the pore, and size of nanocrystals (19–22). These advantages of MOFs have led to various applications including lithium-ion batteries, gas-vapor separation, gas storage, and catalysis (23–25). The MOF abilities, particularly its excellent trapping and releasing molecules of interest, are extremely advantageous for biological studies (26–28). Specifically, several essential biomolecules, including bulk metals (e.g., potassium, calcium, and magnesium), trace metals (e.g., zinc, iron, and manganese), amino acids, neurotransmitters, and even vitamins, can be stored and constantly released from the MOFs over a long period of time (28–32). Therefore, such biomolecule-embedded MOFs can be extremely useful for controlling stem cell fates, which partially replace the role of the surrounding 3D cellular microenvironment in vivo. However, to realize the full potential of MOFs as a stable differentiation factor supplier, physical contact between the cells and MOFs, including their uptake into the cytosol, should be avoided to prevent structural deformation of the MOFs and to avoid potential cytotoxicity or adverse effects of the MOFs on target cells.

Here, we report a new type of platform that is referred to as single nanocrystalline MOF (nMOF) nanoparticle–embedded nanopit arrays (SMENA) that are capable of guiding one of the most important differentiation lineages of stem cells, neurogenesis (Fig. 1). First, nMOF, termed nUiO-67, was synthesized and characterized for stable RA storage and long-term release (>26 days). Thereafter, to prevent any physical interaction between the cells and nUiO-67 and to enhance cellular adhesion on substrates, large-scale homogeneous nanopit arrays were generated using laser interference lithography (LIL) (33–37). By adjusting the size of the nanopits to approximately 450 nm with a 250 nm gap distance ($L_{hole}/L_{pitch} = 0.64$) and considering the diameter of nUiO-67 as approximately 177 nm, we can confine one nanopit with one nUiO-67 nanoparticle with 98.3% loading efficiency. As a proof of concept, neural stem cells (NSCs; NE-4C) were chosen, which are capable of differentiating into neuronal cells under RA treatment. Owing to the stable RA supply from the underlying

[1]School of Integrative Engineering, Chung-Ang University, 84 Heukseuk-ro, Dongjak-gu, Seoul 06974, Republic of Korea. [2]Department of Chemical and Biological Engineering, Sookmyung Women's University, 100 Cheongpa-ro 47-gil, Yongsan-gu, Seoul 04310, Republic of Korea. [3]Department of Biomedical Engineering, SKKU Institute for Convergence, Sungkyunkwan University (SKKU), Suwon 16419, Republic of Korea. [4]Department of Intelligent Precision Healthcare Convergence, SKKU Institute for Convergence, ungkyunkwan University (SKKU) , Suwon, Gyeonggi 16419, Republic of Korea. [5]LabInCube Co. Ltd., A304-C2, 45, Yangcheong 4-gil, Ochang-eup, Cheongwon-gu, Cheongju-si, Chungcheongbuk-do, Republic of Korea.
*Corresponding author. Email: kmchoi@sm.ac.kr (K.C.); thkim0512@cau.ac.kr (T.-H.K.)
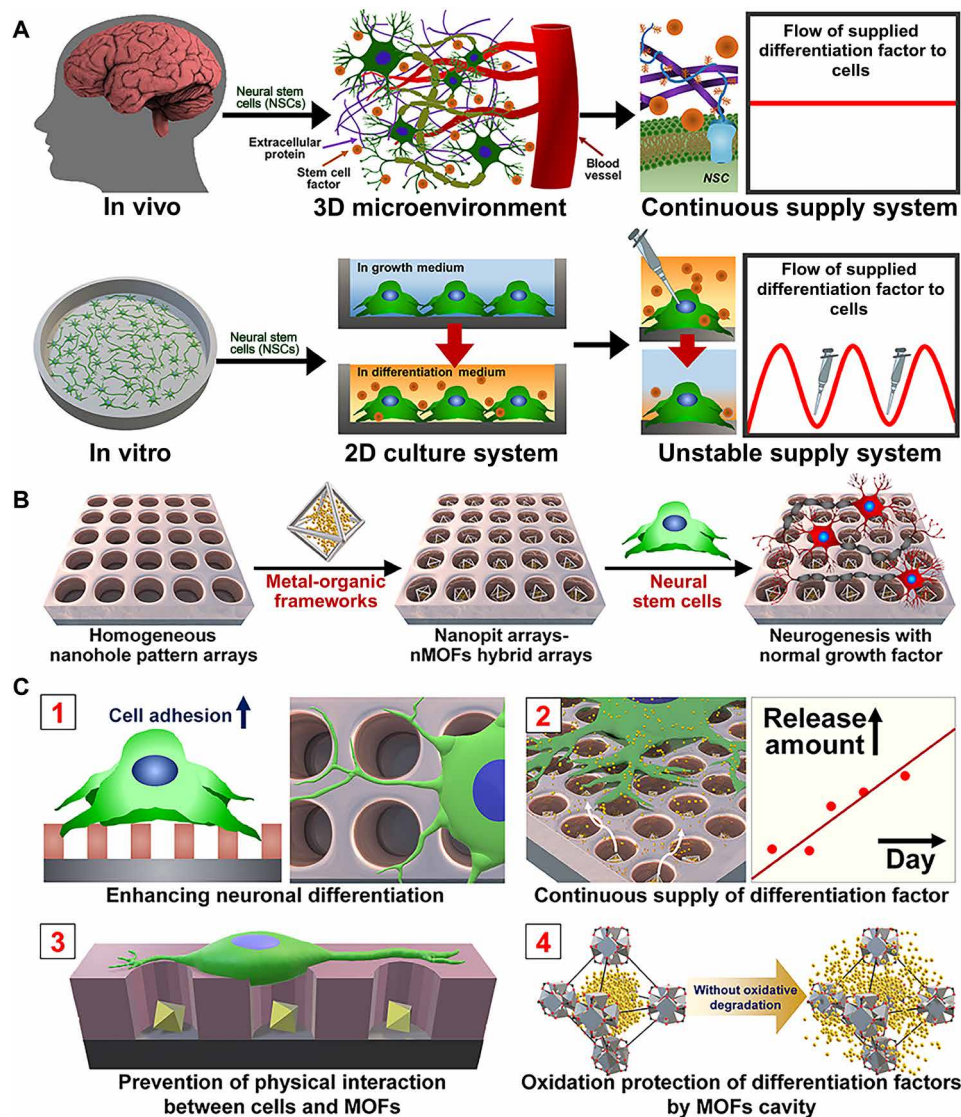†These authors contributed equally to this work.

Fig. 1. Schematic illustration of SMENA. (A) Most critical difference between real in vivo and in vitro environments. The in vivo environment is based on three-dimensional (3D) structures where the living cells can be continuously supplied with various nutrients on time and demand, whereas in vitro cells rely on the unstable nutrient supply system. **(B)** Single RA-containing metal-organic framework (MOF)–embedded nanopit arrays (RA-SMENA) consist of RA-containing nanocrystalline UiO-67s (RA-nUiO-67) and nanopit arrays with highly homogeneous nanoarrays, which function as a continuous and stable nutrient supply system for enhancing the neurogenesis of the NSCs. **(C)** RA-SMENA has several advantages for grafting MOFs into the 2D culture system and eventually accelerating the neurogenesis. First, the nanopit arrays can guide and support the neuronal differentiation of the NSCs. Second, the RA-SMENA can continuously supply RA to the NSCs for a long period, which enables the RA-SMENA to achieve neurogenesis without any additional treatment of a differentiation factor. Third, the nanopit array prevents the interaction between RA⊂nUiO-67 and the cells, which allows them to maintain both the structures and functions of RA⊂nUiO-67. Fourth, chemical decomposition of the RA located inside RA⊂nUiO-67 can be prevented. These above-mentioned advantages have a synergistic effect in driving the enhancement of neurogenesis through realizing in vivo properties in the 2D culture system.

RA⊂nUiO-67 and the prevention of chemical isomerization of RA in the RA⊂nUiO-67 pores, in vitro neurogenesis of NSCs was significantly enhanced and accelerated compared to all other control groups, including the conventional differentiation method.

RESULTS
Design, synthesis, and characterization of RA⊂nUiO-67 for RA storage and long-term release

The nMOF chosen for this study is $Zr_6O_4(OH)_4(BPDC)_6$ [(BPDC, 4,4′-biphenyldicarboxylate), UiO-67] since it grows as monocrystalline

nanoparticles and is chemically stable for a long period of time (*19, 38*). We hypothesized that the microporosity of nUiO-67 will contribute to the massive absorption of RA via capillary action in an RA-rich solution and will enable the sustained release of RA due to the slow kinetics of diffusion among the pores (Fig. 2A). The scanning electron microscopy (SEM) images of nUiO-67 showed uniform size (ca. 177 nm) (Fig. 2, B and D) and exhibited truncated octahedron geometry in the particles (Fig. 2C). The crystallinity of nUiO-67 is evident from the diffraction lines that match those of the simulated pattern for the UiO-67 structure (Fig. 2E) (*38*), and the permanent porosity was confirmed by measuring the N_2 gas adsorption isotherm (Fig. 2F).

The absorption and release behaviors were characterized by measuring the amount of RA in the solution containing the nUiO-67 particles. The amount of RA absorption was quantified by measuring the difference in the RA amount after immersion of nUiO-67 from the prequantified stock solution (Fig. 2G). nUiO-67 exhibited an initial uptake of a large amount of RA from the solution in an hour, which is referred to as RA⊂nUiO-67, and then did not get absorbed any further up to 10 hours. The amount of total RA uptake in

RA⊂nUiO-67 was 26×10^{-5} mmol mg^{-1}. The particles were immersed in the pure solvent, and the amount of RA released from RA⊂nUiO-67 was measured for 2 weeks with a 2-day time interval. RA⊂nUiO-67 initially released RA at a rate of 6.6×10^{-5} mmol mg^{-1} per day for the first 2 days and then was stabilized to release RA at 0.7×10^{-5} mmol mg^{-1} per day for the final 24 days (Fig. 2H). It is speculated that the initial fast release was caused by some of the RA molecules remaining outside the RA⊂nUiO-67 particles. We repeated
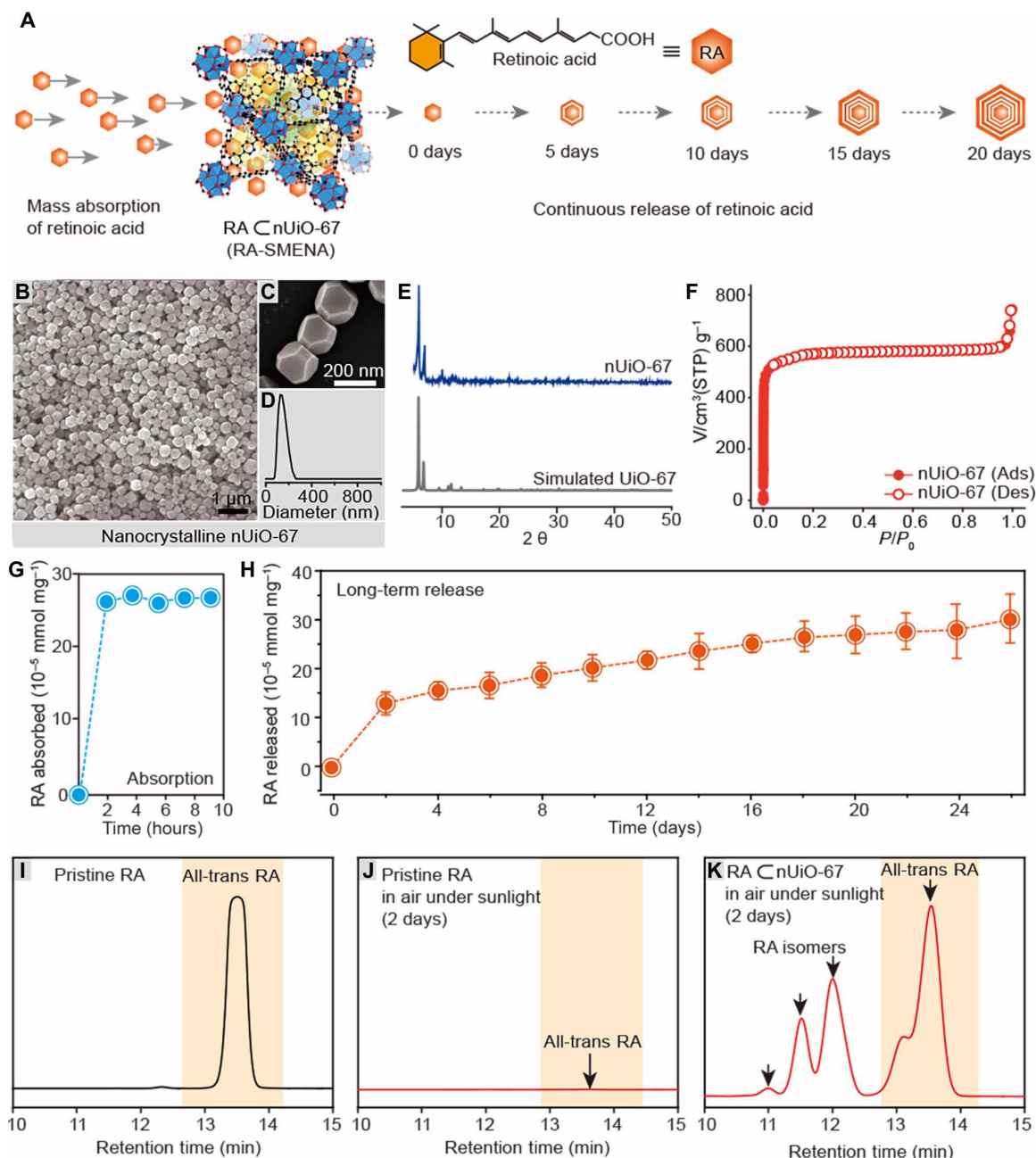

Fig. 2. RA⊂nUiO-67 synthesis and characterization. (**A**) Schematic illustration showing massive absorption of RA to nUiO-67 and the continuous release of RA from RA⊂nUiO-67. (**B** and **C**) SEM images for the nUiO-67 particles at ×11,000 and ×100,000 magnifications. (**D**) Particle size distribution of the nUiO-67 particles measured by dynamic light scattering. (**E**) Powder x-ray diffraction (PXRD) patterns of nUiO-67 compared to the simulated pattern of UiO-67. (**F**) N$_2$ adsorption isotherms at 77 K with adsorption and desorption points represented by closed and open circles, respectively (P/P_0, relative pressure). (**G**) RA absorption curve in nUiO-67 over time. (**H**) RA release curve from RA⊂nUiO-67 for 26 days at 2-day intervals. (**I** to **K**) RA spectra measured through HPLC for pristine RA and RA⊂nUiO-67.

the long-term RA release measurements several times and confirmed that the amount of RA released continuously increased in the range shown as error bars in Fig. 2H.

An important factor that warrants further examination is the stability of RA captured inside the nUiO-67 pores. It is known that RA molecules can be easily isomerized and will lose their original structure within a day (*39*, *40*). Therefore, in the conventional differentiation methods, exchanging spent RA with the freshly stored one under low temperature has been a regular requirement (*41*, *42*). We tested the stability of RA inside nUiO-67 by comparing it with pristine RA. In the high-performance liquid chromatography (HPLC) spectra for all-trans RA (Fig. 2I), no peak was initially found for pristine RA (Fig. 2J) but was clearly observed for RA⊂nUiO-67 (Fig. 2K) after being exposed for 2 days in air under sunlight. This indicates that the original all-trans RA structure was preserved in the pores of RA⊂nUiO-67. Other peaks were found at retention times of 11 to 13 min, which can be attributed to the partially isomerized RA (fig. S2) (*42*). This evidence coupled with the long-term release of RA from RA⊂nUiO-67 observed in Fig. 2H supports the notion that the RA inside the nUiO-67 pores remains unchanged and only deteriorates upon release. Therefore, RA⊂nUiO-67 can preserve the chemical structure of RA inside its pores and quantitatively releases its original form for an extended time of up to 26 days.

Fabrication of SMENA

After the confirmation of the excellent properties of RA⊂nUiO-67 for long-term and stable RA release, we attempted to load single nUiO-67 on the platform for spontaneous neurogenesis of stem cells. To achieve this, nanopit arrays that are proven to be biocompatible and effective for cell adhesion were fabricated as a template for loading RA⊂nUiO-67. The dimensional specifications of the nanopit arrays were adjusted such that the hole diameter of nanopit arrays was 450 nm, pitch size was 700 nm, and height was 710 nm, with a size variation of ±5% (Fig. 3, A to C), which is optimum for trapping RA⊂nUiO-67. Besides optimizing the dimensional parameters of nanoarrays for uniform RA⊂nUiO-67 loading, we also further adjusted the coating conditions, including nUiO-67 concentrations, spin-coating speed, and the nUiO-67 dispersion solvent (fig. S4 to S6). As shown in Fig. 3D, significant uniformity of RA⊂nUiO-67 loading on the nanopits, i.e., one RA⊂nUiO-67 per nanopit, can be achieved on the entire cell cultivation platform. The percentage of single RA⊂nUiO-67 in a single nanopit was calculated as 98.3% based on multiple high-magnification SEM images (Fig. 3E). In addition to the homogeneity of the nanopit arrays and uniformity of the nUiO-67 loading, the film thickness of the nanopit arrays is a critical parameter to prevent physical interactions between the cell membrane and nUiO-67. The pseudo-colored SEM cross-sectional images (Fig. 3F) and atomic force microscopy (AFM) images (Fig. 3G) also revealed that the height of the nanopits is approximately 710 nm, which is sufficient for the isolation of nUiO-67 from an external environment including cells. Next, to fully confirm the presence of nUiO-67 in the nanopit structure, energy-dispersive x-ray spectroscopy (EDX) mapping was performed. We found that the peak representing the major component of the synthesized nUiO-67, zirconium, specifically appeared on the nUiO-67 nanoparticles existing inside the nanopits. The underlying substrate, that is, the indium tin oxide (ITO)–coated glass substrate, showed both Si- and In-specific peaks for the entire nanopit's circular area. Besides, similar to RA⊂nUiO-67 dispersed in the solution, the RA⊂nUiO-67

nanoparticles embedded in nanopit arrays also showed a stable RA release profile for initial 24 hours, proving its functionality as an RA-supplying cell culture platform (fig. S6). Together, it can be concluded that single RA⊂nUiO-67 nanoparticles were successfully loaded, homogeneously distributed, and isolated from the external environment on the whole nanoarray area (110 × 110 mm), which is essential for the stable and long-term supply of RA to the NSCs that will be attached and grown at the top of the nanopit arrays.

Biocompatibility and long-term stability of SMENA

The biocompatibility of the platform in which cells attach, grow, and differentiate should be guaranteed before its usage for cell culture. First, the multipotency of the NSCs grown on the SMENA was studied since it is one of the most important characteristics of stem cells. Three different types of platforms, including bare ITO, nanopit arrays, and nUiO-67 in nanopit arrays, were fabricated and tested. A bare ITO-coated glass substrate was chosen as a basic supporting plate and used as a control group since its excellent electrical property was proven to be advantageous for enhancing neurogenesis. As shown in Fig. 4 (C and D), no meaningful differences were found for all the groups regardless of the passage (passages 5 to 7), based on the mRNA expression levels of both *Nestin* and *sex-determining region Y–box 2* (*SOX2*) (Fig. 4, E to G), which indicates that the nanopit arrays and nUiO-67 did not negatively affect the differentiation potential of the NSCs. Besides, owing to the increase in the cell adhesion, one major NSC behavior, proliferation, was enhanced by 115 and 203% on the nanopit arrays and SMENA, respectively, as compared with bare ITO at day in vitro (DIV) 2 and DIV 4, respectively (fig. S7). The results are consistent with our previous study reporting the positive effects of nanopit arrays on stem cell growth. Last, the long-term stability of the nUiO-67 nanoparticles trapped in the nanopits was confirmed in the presence of the NSCs and culture medium. As shown in Fig. 4H, the nUiO-67 nanoparticles remained undamaged and stably located for the long-term cultivation period (>DIV 7), owing to the prevention of physical contact with cells, which is a perfect feature for prolonged RA supply. No nanoparticle uptake of NSCs was observed during entire cultivation and differentiation period as confirmed by energy-dispersive x-ray spectroscopy (EDS) analysis after cell lysis (fig. S8). Together, the SMENA platform is capable of long-term culture of the NSCs without hampering their growth and differentiation potential and can retain the RA⊂nUiO-67 nanoparticles for a long period of time. Therefore, it can be concluded that the SMENA platform is suitable for inducing neurogenesis on the platform without adding extrinsic differentiation factors into the medium.

Neurogenesis of NSCs on RA-SMENA with growth medium

After the confirmation of biocompatibility and long-term stability of the SMENA, neurogenesis was induced (fig. S10). As a proof of concept, a mouse NSC (NE-4C) capable of differentiating into neuronal cells under RA treatment was chosen as the model cell line. For control groups, the NSCs were first subjected to RA treatment after 2 days of culture for metabolic stabilization (Fig. 5A). RA is highly unstable under typical cell cultivation conditions and must therefore be freshly prepared every 2 days during the medium change for the entire differentiation period (14 days). In the case of the NSCs cultured on single RA-containing MOF-embedded nanopit arrays (RA-SMENA), the experimental procedure is completely different from the conventional methods. Owing to the presence of RA⊂nUiO-67 that continuously supplies RA to the cells, only a
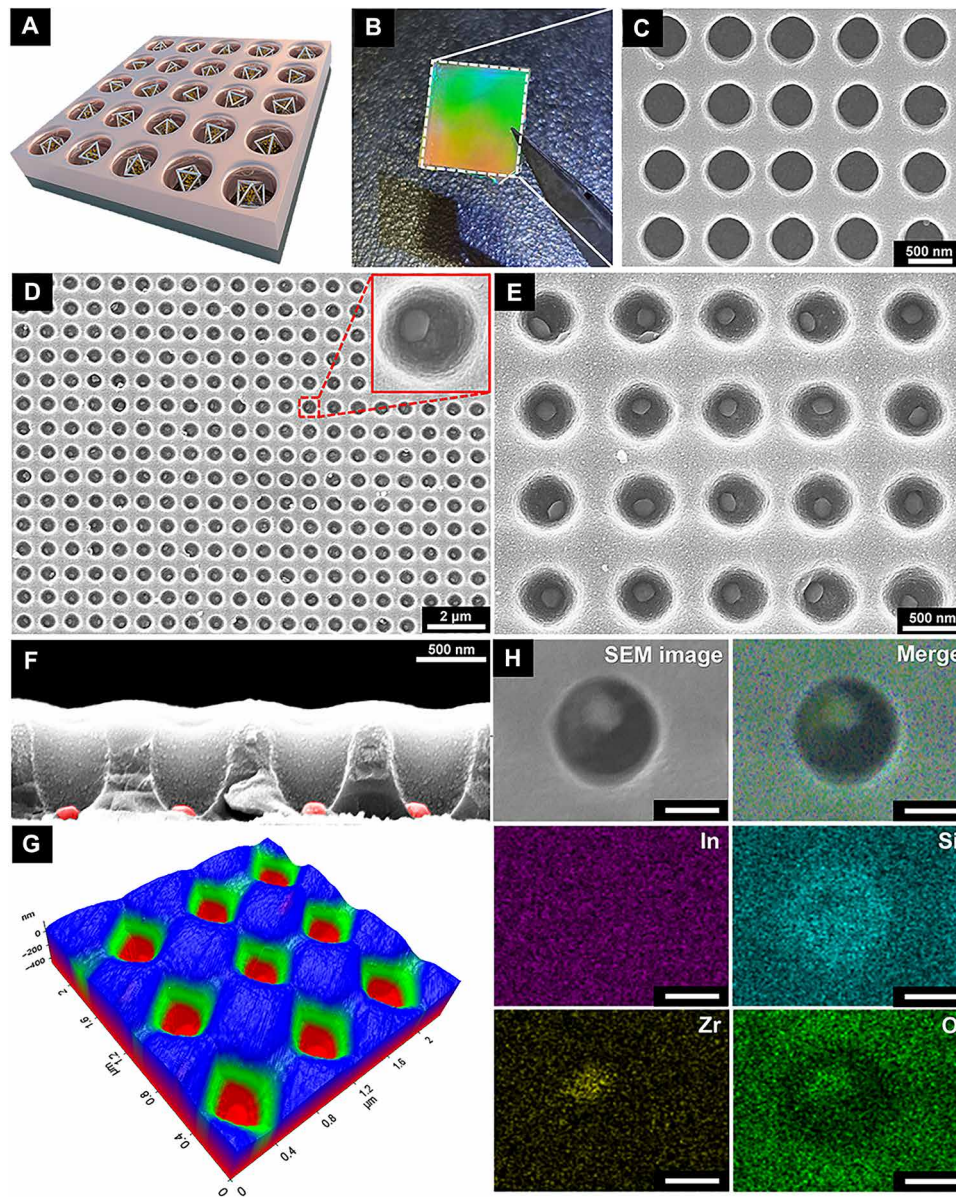
Fig. 3. Characterization of SMENA. (**A**) Schematic illustration showing the structure of SMENA. (**B**) Real picture of the large-area nanopit arrays (12 mm × 12 mm) fabricated by the LIL processes. (**C**) Top view of the nanopit array with the desired dimensions (hole: 500 nm, pitch: 800 nm, and height: 708 nm) in terms of the optimum effect for supporting the neurogenesis. (**D**) Top view of the SMENA fabricated with the optimized conditions of the RA⊂nUiO-67 coating. The red box-shaped indicator represents the enlarged images of a single SMENA where a single RA⊂nUiO-67 is located on the base of the nanopit. (**E**) Enlarged SEM image of the SMENA fabricated with the optimized conditions of the RA⊂nUiO-67 coating. (**F**) Cross-sectional view of the SMENA showing the location of RA⊂nUiO-67s in the SMENA. To clearly indicate the positions of RA⊂nUiO-67s, they are pseudo-colored. (**G**) AFM images of the SMENA showing its entire structure. (**H**) EDX analysis of the SMENA to chemically prove whether the particles coated onto the base of nanopit arrays are RA⊂nUiO-67s. Total four representative elements—indium, silicon, zirconium, and oxygen—are used in the EDX analysis. Scale bars, 500 nm.

typical growth medium was used and replaced every 2 days without external RA addition. At DIV 7, the Nestin expression (i.e., NSC marker) was lower on the RA-SMENA, while Tuj1 and microtubule-associated protein 2 (MAP2) marker expressions were 1.12 and 1.14 times higher than the control group (i.e., NSCs treated with typical neural induction medium), respectively (fig. S11). At DIV 14, the MAP2 expression had increased 2.55 times on the RA-SMENA compared to the control group, while Nestin and premature neuronal marker (Tuj1) decreased significantly (Fig. 5, C and D, and fig. S12).

Relative marker expression analysis also showed remarkable results, indicating that 35.02% of differentiated cells on the RA-SMENA express MAP2, while only 7.93% of the control cells were positive for MAP2 staining (Fig. 5E). Neither neurosphere formation nor neuronal cell generation was observed from the NSCs cultured with a typical growth medium on both bare ITO and nanopit arrays (figs. S13 and S14). This finding indicates that the RA-SMENA is extremely effective in the rapid neuronal maturation of the NSCs with high neural conversion efficiency. To further prove that this early
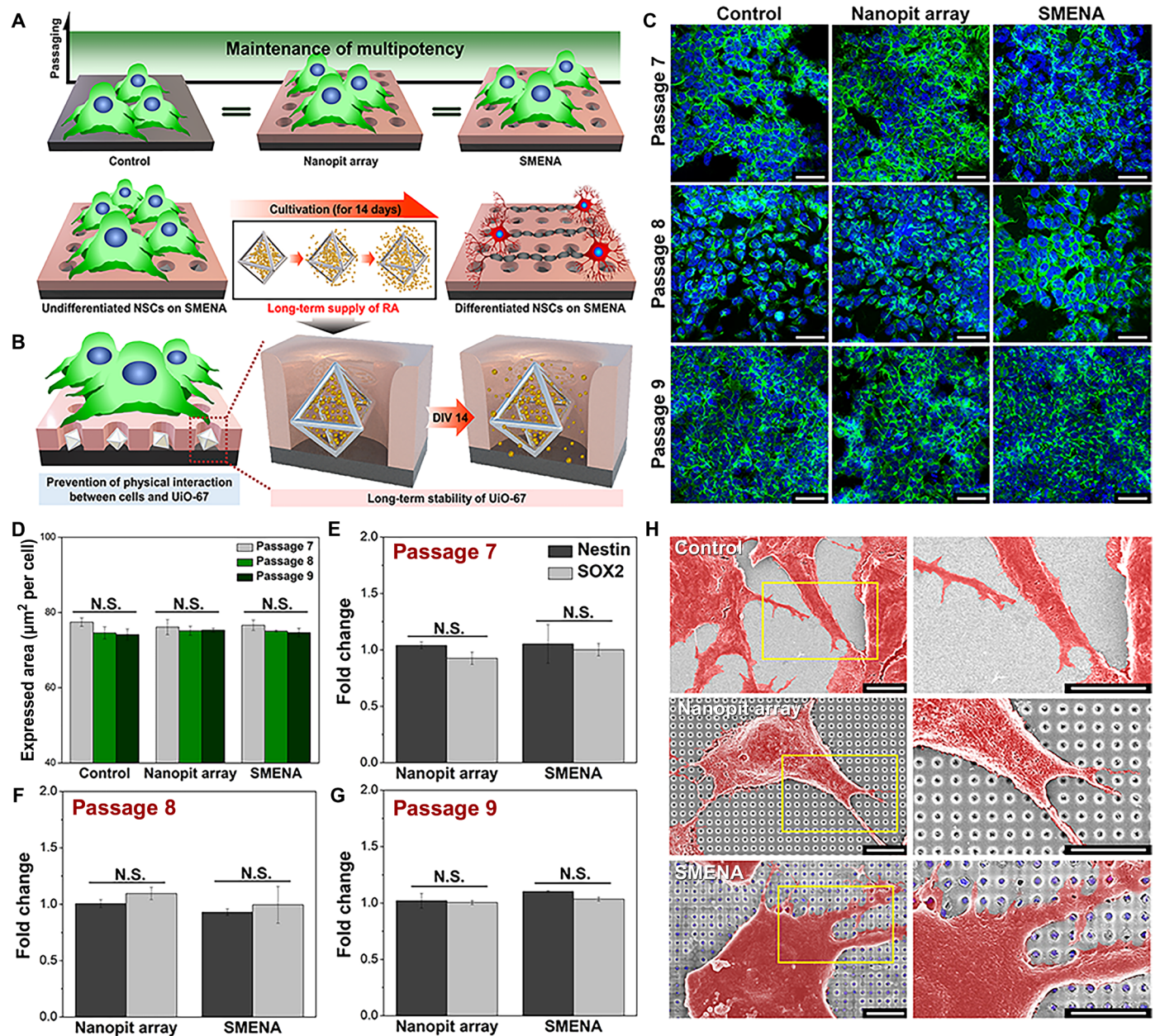
Fig. 4. Monitoring the multipotency of the NSCs cultured onto each group at several passages. (**A**) A schematic illustration showing multipotency of the NSCs at each passage as a starting point of neural differentiation. (**B**) A schematic illustration indicating favorable merits, including (i) prevention of physical interactions between the cells and nUiO-67 and (ii) long-term stability of nUiO-67. (**C**) Immunocytochemistry images of the NSCs maintained onto each group at passages 7 to 9. The NSCs were stained with Nestin (green) and Hoechst (blue). Scale bars, 50 μm. (**D**) Quantitative analysis of immunocytochemical images obtained from (C); N.S. indicates "not significant." (**E** to **G**) RT-qPCR results of the NSCs cultured onto each group at several passages; the data were normalized to the control. (**H**) SEM images of the NSCs cultured on each group at passage 7 and day 4. The SEM images in the second column are the enlarged images obtained from the area indicated by the red box–shaped indicators in the first column. Scale bars in the first and second columns are 10 and 1 μm, respectively. Statistical significance was obtained from unpaired Student's *t* test; *n* = 3.

initiation of neurogenesis and maturation is not induced by simple early exposure to RA, the NSCs undergoing differentiation were categorized into two groups: (i) typical induction (normal) and (ii) RA-SMENA–like induction (early) methods. In the early induction method, the NSCs were treated with an RA-containing medium immediately after seeding (fig. S15). As a result, the neurosphere generations were observed from all groups on day 2; however, they failed to maintain a clear spherical morphology and gradually degraded, regardless of the type of platform applied, indicating that the early induction method is inappropriate for accelerating and enhancing the neurogenesis of the NSCs (figs. S16 and S17). Further study also revealed that neurogenesis was suppressed when NSCs were treated with high concentrations of RA for both normal and early induction models (fig. S18).
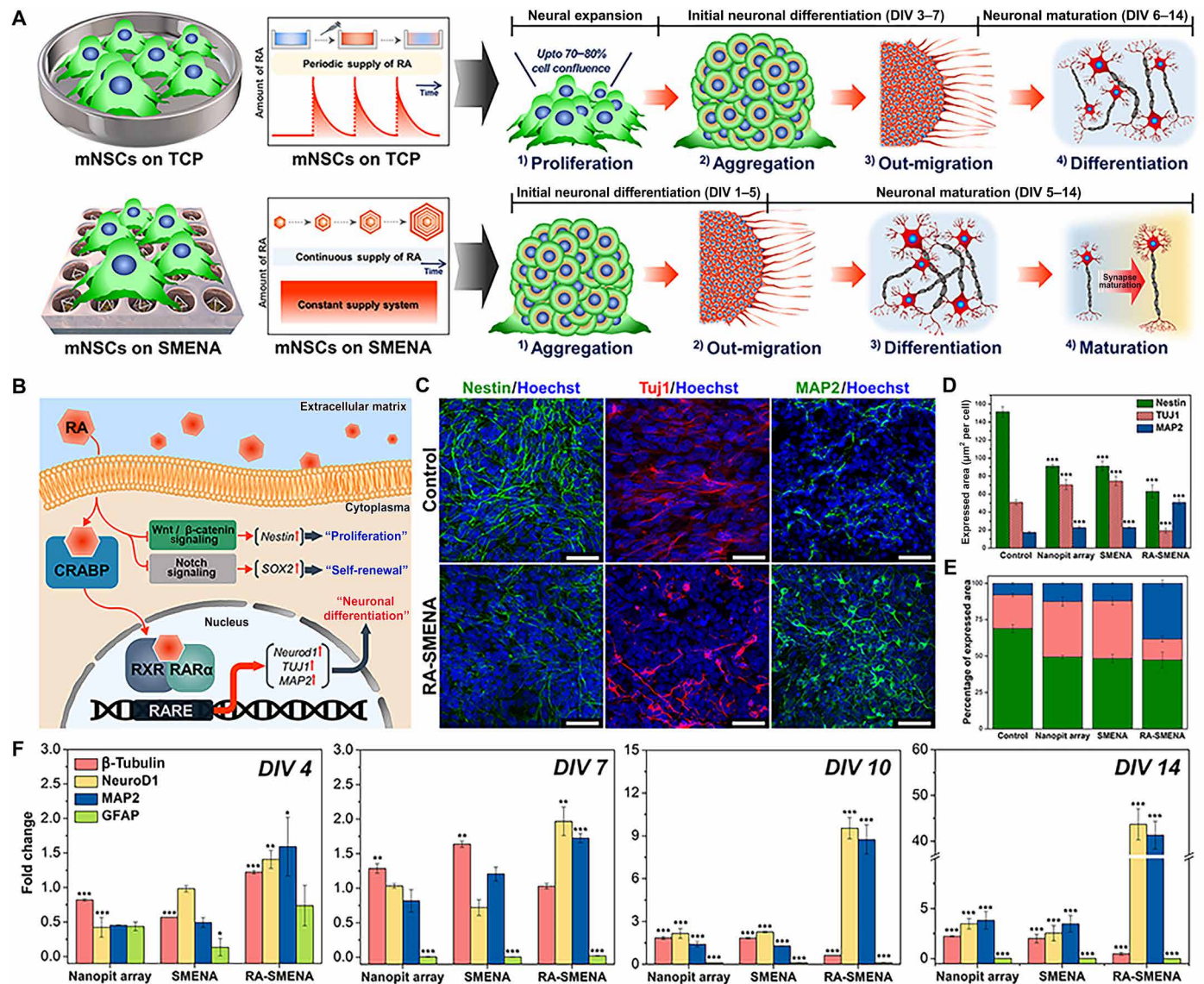
Fig. 5. Analysis of genes and proteins related to neurogenesis. (**A**) A schematic illustration showing different differentiation mechanisms between the control group and RA-SMENA. (**B**) A diagram indicating RA signaling pathways, including its downstream transcription factors, and therefore its up-regulated or down-regulated genes. (**C**) Immunocytochemistry-based analysis of neurogenesis of each group at 14 days. Scale bars, 50 μm. (**D** and **E**) Quantitative analysis and relative percentage of protein expression obtained from (C) and fig. S12. "Expressed area (μm² per cell)" indicates the expression area of each target protein per the number of nuclei indicating the number of cells in each image. "Percentage of expressed area" means the relative percentage of specific protein expression compared to the total expression levels of target proteins in each group. The data were normalized to the control. (**F**) RT-qPCR results of the NSCs from each group at days 4, 7, 10, and 14, respectively; the data were normalized to control. *$P < 0.05$, **$P < 0.01$, and ***$P < 0.001$.

To further prove the excellence of SMENA in terms of guiding neurogenesis, the mRNA expression levels of multipotency markers (e.g., *Nestin* and *Sox2*), early neuronal marker (*Tuj1*), mature neuronal markers (e.g., *NeuroD1* and *MAP2*), and *astroglial marker* [glial fibrillary acidic protein (*GFAP*)] were analyzed at DIV 4, DIV 7, DIV 10, and DIV 14 (Fig. 5F and figs. S19 and S20). As a result, the expression levels of *NeuroD1* and *MAP2* were significantly increased on the RA-SMENA when compared with both the nanopit array and SMENA at DIV 7 (Fig. 5F). The difference between the RA-SMENA and other groups in terms of neural cell marker expression became more significant at DIV 10. Specifically, the expression level of *NeuroD1*, a key transcription factor responsible for

converting reactive glial cells into functional neurons, was 9.54 times higher on the RA-SMENA than the normal induction group (control), while the *MAP2* expression was 8.75 times elevated on the same platform. The relative mRNA expression levels of *NeuroD1* and *MAP2* on RA-SMENA were 43.7 and 41.3 times higher than the normal induction group and cannot be compared with the nanopit arrays and SMENA groups in terms of the neurogenesis efficiency. On the basis of the relative percentage of the *MAP2* gene expression, we found that the *MAP2* expression of the cells on the RA-SMENA was approximately 50%, while the *Tuj1* expression was calculated to be <1% among all the three genes tested (fig. S20). Such an extremely low *Tuj1* expression is completely different from other groups as

the *Tuj1* expressions of the NSCs on both the nanopit arrays and SMENA were found to be 23 to 25% at DIV 14. To further prove the outstanding performance of RA-SMENA as a platform to enhance neurogenesis at protein expression levels, flow cytometry analysis was performed using Nestin, Tuj1, and MAP2 antibodies (fig. S21). As a result, 78.26, 92.01, and 98.30% of the cells cultured on the RA-SMENA were found to be positive for Nestin, Tuj1, and MAP2, respectively, while 75.05, 86.45, and 84.64% of the control cells were positive for the same three markers. The dynamic neuronal activities were also confirmed by Ca^{2+} influx study using Fluo-4am as a fluorescence indicator (movie S1).

To comprehensively understand the effect of the RA-SMENA on the transcriptome involved in the neurogenesis of the NSCs, RNA sequencing was performed with the NSCs cultured on each group over 14 days (Fig. 6A and fig. S22). As shown in Fig. 6A, among 23,284 genes, 1774 were identified to be related to neurogenesis, and their up- or down-regulation was analyzed as shown in the heatmap clustering with a dendrogram. We found that among the 194 genes identified as upregulated, the number of genes that showed significant increases were 7, 22, and 172 for the nanopit array, SMENA, and RA-SMENA, respectively, while the average fold changes of the upregulated genes were found to be 2.55, 2.56, and 15.0 for each group, respectively (tables S2 and S3). The scatterplots and volcano plots obtained from Database for Annotation, Visualization and Integrated Discovery analysis also revealed that the gene expression levels of the NSCs differentiated on the RA-SMENA were significantly different from other groups (Fig. 6, B and C, and fig. S22). In the case of comparison between the nanopit array, SMENA, and RA-SMENA, 1153 genes related to neurogenesis were selectively up-regulated in the RA-SMENA, indicating that the RA-SMENA is extremely efficient for both enhancing neurogenesis and neuronal maturation (Fig. 6D). Likewise, the detailed cellular activity related to neurogenesis was analyzed (Fig. 6, E to G). First, the gene expressions related to the control of NSC maintenance (i.e., negative regulation of neurogenesis: Draxin, Damm2, and Kctd1l; negative regulation of neuron projection development: Fat3, Dpysl3, and Nr2f1) were decreased in the RA-SMENA group (Fig. 6E and table S3). However, the genes closely associated with the neurogenesis (total: 372 genes) were significantly up-regulated, including axon guidance/extension, dendrite development, neuron migration, synaptogenesis, and neuron maturation (Fig. 6, F and G, and table S4). We further confirmed that several RA-related cellular activities increased, including *cellular retinoic acid-binding protein 1* (*CRABP*), *retinoid X receptor* (*RXR*), and *retinoic acid receptor alpha* (*RAR-α*), which are responsible for the up-regulation of key neuronal differentiation (e.g., *NeuroD1*, *Tuj1*, and *MAP2*) (Fig. 5B). This finding proves that the NSCs on the RA-SMENA were exposed to RA continuously and were thus effectively differentiated into neuronal cells.

DISCUSSION

We developed SMENA for controlling neurogenesis in vitro. The nUiO-67 nanoparticles can load RA within a short incubation time (<48 hours) and were capable of releasing RA for a long period of time (>14 days). The RA⊂nUiO-67 cavity also showed excellent performance in protecting RA from degradation and isomerization despite its instability in conventional culture conditions. The
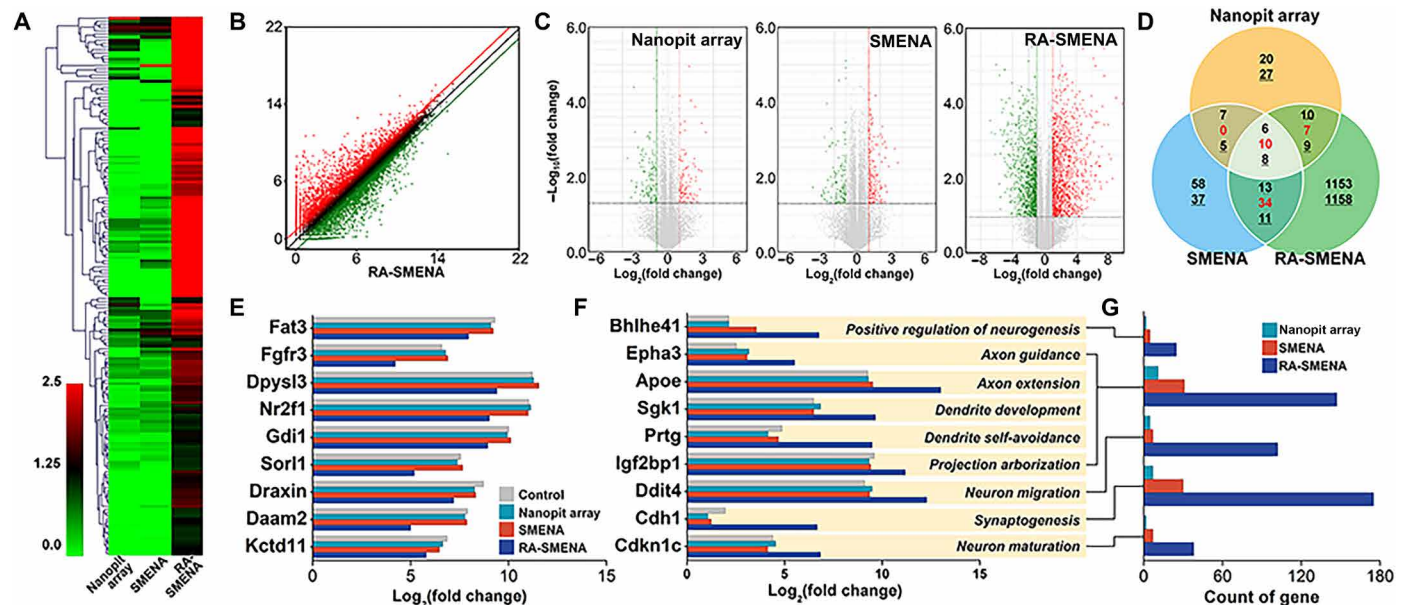

Fig. 6. Analysis of total mRNA expressions of differentiated cells from NSCs. (**A**) Heatmap clustering with a dendrogram of significantly up-regulated genes associated with neurogenesis in each group [fold change > 2, normalized data (log₂) > 4, P < 0.05, n = 3]. (**B** and **C**) Scatterplot of the RA-SMENA and volcano plots of each group. The red and green points on the plot indicate the significantly up-regulated and down-regulated genes compared to the control group, respectively (P < 0.05, fold change > 2.0); the black points indicate expressed genes with no difference compared to the control. (**D**) Venn diagram showing the numbers of up-regulated or down-regulated genes across each group. The black letters, underlined letters, and red letters indicate up-regulated genes, down-regulated genes, and contraregulated genes, respectively. (**E** and **F**) Gene ontology (GO) term analysis of up-regulation of representative genes involved in negative and positive neurogenesis (P < 0.05 and fold change > 2.0), respectively. (**G**) Quantification of the number of neurogenesis-associated up-regulated genes in each group, for which the number of up-regulated genes in each group for each categorized neuron development was quantified. Statistical significance was obtained from unpaired Student's t test; n = 3.

homogeneous nanopit arrays were extremely effective at trapping single RA⊂nUiO-67 particles (i.e., single RA⊂nUiO-67s per nanopit: 98.3%). RA⊂nUiO-67 in the nanopits was stable for a long cultivation period due to the prevention of cellular uptake and could control the neurogenesis of mouse NSCs without harming their multipotency. The expression levels of *NeuroD1* and *MAP2*, the representative markers of mature neurons, on the RA-SMENA were 43.67 and 41.3 times higher than those in the cells that undergo differentiation on tissue culture plates with a conventional differentiation medium. Moreover, approximately 1153 genes related to neurogenesis were selectively up-regulated in the RA-SMENA, most of which are linked to RA-mediated neuronal differentiation based on the KEGG pathway analysis.

Since the RA⊂nUiO-67 nanoparticles can be restructured to load different types of biomolecules (e.g., caffeic acid, minoxidil, and ascorbic acid) by controlling the pore size, pore volume, and particle size of the nMOF, the potential of the developed platform is extremely high. Specifically, pluripotent stem cells can be converted into desired cell types in a more efficient and convenient manner using multiple differentiation factor-loaded SMENA platforms. Moreover, the spontaneous multilineage differentiation from the same stem cell sources could be realized using advanced SMENA platforms. Therefore, we can conclude that the developed SMENA platforms have a wide application potential and are thus promising in stem cell–based regenerative therapies.

MATERIALS AND METHODS

Synthesis of nUiO-67

nUiO-67 as nano-sized RA⊂nUiO-67s was prepared by dissolving zirconium (IV) chloride (0.035 g, 0.15 mmol) and biphenyl-4,4′-dicarboxylic acid (0.018 g, 0.075 mmol) in *N,N′*-dimethyl formamide (10 ml) and acetic acid (0.69 ml) while adding trimethylamine (60 μl). The solution was sonicated for 10 s and reacted at 120°C in a heating block for 18 hours. After that, the mixture was collected by centrifugation (6000 rpm, 10 min) and washed with *N,N′*-dimethylformamide and methanol three times. After washing, the product was dried in a vacuum oven.

Fabrication of nanopit arrays

To fabricate homogeneous nanopit arrays, we used LIL, a nano-patterning technique, with a Lloyd's mirror as an interferometer system. To prepare LIL, the ITO-coated glass (size: 12 mm × 17 mm; thickness: 0.7 mm; electrical resistivity: 10 ohms) was first washed with a series of cleaning processes, followed by sequential sonication treatment with 1% Triton-X, distilled water, and 70% ethanol, respectively, for 20 min. Thereafter, the cleaned glass was treated by heating at 100° to 140°C for >5 min to dry it thoroughly. After heating, the glass was modified with hexamethyldisilazane (HMDS) using a spin-coating technique (1000 rpm, 1000 rpm/s, and 15 s) to make its surface hydrophobic and increase the adhesion between the photoresist (PR) and glass. After the modification, the modified glass was coated with negative PR diluted with thinner (PR:thinner = 6:4) using the spin-coating technique (4000 rpm, 166.7 rpm/s, and 84 s) such that the height of the PR layer was 600 to 650 nm. Then, the PR-coated glass was soft-baked by heating (130°C and 1 min) to eliminate the organic solvent within the PR layer. Thereafter, the PR-coated glass was exposed twice to ultraviolet (UV) laser (wavelength: 325 nm; power: 10 mV) by rotating it clockwise. To fabricate large-scale homogeneous nanopit arrays with the desired dimensions,

the nanopit size was determined via the optimization process between the nanopit size and several parameters (e.g., laser intensity and exposure dose). The pitch of the nanopit arrays was fine-tuned by controlling the angle of the UV laser to Lloyd's mirror based on the theoretical calculations provided below

$$P = \lambda \text{ (UV laser)}/2\sin(\theta)$$

where P, λlaser, and θ indicate the pitch of each nanopit array (nm), the wavelength of the UV laser (nm), and the incidence angle of the UV laser and Lloyd's mirror (°), respectively. After two exposures, the PR-coated glass was hard-baked by heating (130°C and 1 min) and then treated with a developer for the developing step (2.38% tetramethylammonium hydroxide; 1 min), followed by completely drying water on the surface of the fabricated nanopit arrays. Last, to completely eliminate the remaining unreacted PR, the nanopit arrays were treated with oxygen plasma through a dry-etching process [pressure: 5×10^{-2} torr; gas flow rate: 50 standard cubic centimeters per minute (sccm); plasma voltage: 70 mW; plasma time: 1 min].

Fabrication of RA-SMENA

Ensuring RA absorption in the nUiO-67 pore space requires several processes. First, nUiO-67 stored in 70% ethanol was sonicated for 20 min to ensure that the nanoparticles were evenly dispersed. Then, RA⊂nUiO-67s were washed with dimethyl sulfoxide (DMSO) via centrifugation (rotational speed: 8000*g*; time: 10 min). Thereafter, the cleaned RA⊂nUiO-67s were immersed in an RA solution diluent with DMSO at 25°C for 48 hours in a state of blocking light. After RA loading, the solvent of RA⊂nUiO-67 was replaced by phosphate-buffered saline (PBS) through centrifugation, which had a concentration of 0.5 mg/ml. Then, to fabricate the RA-SMENA, RA⊂nUiO-67s were coated onto the fabricated nanopit arrays according to several processes. First, the nanopit arrays were treated with oxygen plasma to make their surfaces hydrophilic (pressure: 5×10^{-2} torr; gas flow rate: 70 sccm; plasma voltage: 50 mW; plasma time: 90 s). Thereafter, the RA@RA⊂nUiO-67 solution was dropped and left on the nanopit arrays for 2 min. Next, RA@RA⊂nUiO-67s were dropped on the surface of the nanopit array and left undistributed for 2 min; then, spin-coating was performed under several optimized conditions (maximum rotational speed: 1000 rpm; acceleration: 1000 rpm/s; time: 2 min). Last, additional spin-coating was performed to completely coat RA⊂nUiO-67 that had not settled to the base of the nanopit interior and remove residues of the RA⊂nUiO-67 solution remaining on the nanopit array surface (rotational speed: 2000 to 5500 rpm; time: 1 min).

Characterization of nanocrystalline UiO-67 (nUiO-67) and SMENA

The size and morphology of nUiO-67 were verified by field-emission scanning electron microscope (FE-SEM) with JEM-7600F, JEOL. The powder x-ray diffraction [PXRD; Bruker D8 Advanced (TRIO/TWIN)] spectra were collected at 1600 W (40 kV, 40 mA). The scanning condition was set up with a 6°/min scan rate for 5° to 45° with a silicon holder. Gas adsorption analysis was performed with a BELSORP-max automatic volumetric gas adsorption analyzer. The sample was activated at 110°C for 24 hours before measuring the porosity. Particle size analysis was performed with an SZ-100, HORIBA. The powder was well dispersed using ultrasonication in methanol. For calculating the RA concentration, HPLC analyses

were performed using an Agilent Technologies 1260 infinity II LC system. The column was a 4.6×25 mm Shim-pack GIS C18 (5 μm) (Shimadzu). The mobile phase was a methanol/20 mM phosphate buffer (pH 2.5) (v/v = 90/10) solution mixed by the HPLC pump. The injection volume was 10 μl, and the flow rate was 1 ml/min. The column temperature was 30°C, the detection was 350 nm, and the retention time was 15 min.

To analyze the overall structure of the SMENA and, specifically, the nUiO-67 particles coated on the nanopit arrays, analytical techniques such as FE-SEM (Sigma Family, Carl Zeiss, Germany) and AFM (XE-100, PSIA, South Korea) were conducted with a noncontact mode. Furthermore, to chemically prove that the coated particles on the nanopit array are RA@RA⊂nUiO-67s, EDX was performed on several elements, including common elements, elements specific to ITO substrates, and particularly zirconium (Zr) capable of uniquely labeling nUiO-67s. To confirm the functional structures of SMENA (e.g., no displacement of nUiO-67s from the base of the nanopit interior and no interaction between the cells and nUiO-67s), we split SMENA in half with liquid nitrogen and analyzed its CS image using SEM, which confirmed that the nUiO-67s settled on the underside of each nanopit of the SMENA. Moreover, we compared the position of the nUiO-67s and the height of the nanopit array to confirm the role of the nanopit array as a barrier.

Cultivation and differentiation of NSCs

Before seeding the cells onto the control group and SMENA, several preparation processes were required to culture cells in the desired area of substrates. First, two types of chambers were attached onto the substrates, including control, bare nanopit array, and SMENA, which indicate the areas in which cells are cultured. Specifically, the plastic chambers of 0.78-cm diameter were attached onto all substrates except the SMENA using polydimethylsiloxane (PDMS) blended with a thermal curing agent (ratio 10:1) as a biocompatible glue, and its curing process was performed at 70°C for 30 min. In contrast, to prevent RA⊂nUiO-67 from being exposed to heat, the 0.78-cm-diameter plastic chamber was used as a mold to fabricate a PDMS (ratio 30:1) chamber, and a complex chamber consisting of PDMS was manufactured without removing the plastic chamber. Thereafter, the manufactured composite chamber was attached to the SMENA surface using pressure. Then, all these chamber-attached groups were sterilized with ethanol and UV treatment. Mouse neuroductormal system cells (NE-4C) with passage 5 were obtained from Sogang University (Korea) and cultivated in alpha–minimum essential medium, supplemented with 10% antibiotics, 4 mM L-glutamine, and 10% fetal bovine serum. Before cell seeding, all the substrates in each group were precoated with poly-L-lysine at room temperature for more than 15 min. Then, NE-4C were identically seeded onto each group, including control, nanopit array, SMENA, and RA-SMENA, at 3.62×10^4 cells/cm^2 and cultured under the standard cell cultivation conditions in 5% CO$_2$ at 37°C. To induce neural differentiation in each group, normal growth media without RA was periodically replaced every 2 days on the RA-SMENA, whereas in the other groups including control, nanopit array, and SMENA, differentiation media containing 1 μM RA were periodically replaced every 2 days. In addition, in the case of cells cultured on the RA-SMENA, the day of seeding was considered as the starting point of differentiation because the cells were exposed, and RA was released from the substrate immediately after cell seeding. In contrast, in the other group, the cells were maintained in the normal growth medium until they reached 70 to 80% cell confluence, and then, neural differentiation was initiated in the manner described above. The neural differentiation lasted for 14 days. Neither cell detachment nor reseeding steps were performed during the entire NE-4C growth and differentiation period.

Analysis of cell functions

To analyze the cell viability of the NSCs cultured onto each group, including SMENA, the CCK-8 assay was conducted three times for 6 days. In addition, for in-depth understanding of cell proliferation in each group, the population of dividing cells in each group was analyzed using flow cytometry with bromodeoxyuridine staining. To analyze the morphology of the cells cultured onto each group, the cells were fixed with a 10% neutral-buffered formalin (NBF) solution for 15 min. Then, the cells were dehydrated with 50, 60, 70, 80, 90, and 100% ethanol or HMDS for 15 to 20 min. The dehydrated cells were visualized with FE-SEM. To monitor the multipotencies of the NSCs with several passages (passages 7 to 9) cultured onto the control group, SMENA, and RA-SMENA, immunocytochemistry and a real-time polymerase chain reaction (RT-PCR) were utilized with several genes, including *Nestin* and *Sox2* that are relevant to the multipotency of the NSCs. The NSCs were fixed with 10% NBF solution and subsequently permeabilized with 0.3% Triton X-100. The cells were then incubated with a primary antibody specific to Nestin (1:50; R&D Systems). Subsequently, the cells were washed with PBS and further incubated with goat anti-rat immunoglobulin G H&L (Alexa Fluor 488; Abcam) to visualize Nestin. Hoechst 33342 (Sigma-Aldrich) was used to counterstain the nuclei. All fluorescence images were visualized using a Leica DMi8 confocal microscope (Leica, Germany). To quantify the immunocytochemistry images obtained from the NSCs cultured onto each group with each passage, both the Nestin-stained area and the number of nuclei were calculated using ImageJ software, and the values of the positive area for Nestin per cell were then calculated. The RT-PCR was used to assess the expressions of genes relevant to *Nestin* and *SOX2*. The RT-PCR was conducted in the order of cell lysis, RNA extraction from NSCs, and complementary DNA synthesis. Subsequently, RT-PCR was performed with Synergy Brands (SYBR) Premix Ex Taq (Takara) in StepOnePlus. The threshold cycle values (ΔCt) from the RT–quantitative PCR (qPCR) results were calculated as fold changes based on the Livak method ($2^{-\Delta\Delta Ct}$); the RT-qPCR results were normalized to the gene level of glyceraldehyde-3-phosphate dehydrogenase as a housekeeping gene.

Monitoring the neural differentiation of NSCs

To monitor the neural differentiation of the NSCs, several analytical methods, including immunocytochemistry, RT-qPCR, and flow cytometry [fluorescence-activated cell sorting (FACS)], were performed with several genes or proteins relevant to the differentiation of the NSCs and iPSCs. To analyze the neural differentiation of the NSCs, three proteins, namely, Nestin, class III β-tubulin (Tuj1), and MAP2, which indicated undifferentiated NSCs, immature neurons, and mature neurons, respectively, were analyzed with immunocytochemistry. Furthermore, the two genes (*Nestin* and *SOX2*) relevant to undifferentiated cells and the four genes *Tuj1*, *neurogenic differentiation factor 1* (*NeuroD1*), *MAP2*, and *glial fibrillary acidic protein* (*GFAP*), which indicate immature neurons, intermediate neurons, mature neurons, and glial cells, respectively, were analyzed with the RT-PCR.

SUPPLEMENTARY MATERIALS

Supplementary material for this article is available at https://science.org/doi/10.1126/sciadv.abj7736

View/request a protocol for this paper from *Bio-protocol*.

REFERENCES AND NOTES

1. R. A. Young, Control of the embryonic stem cell state. *Cell* **144**, 940–954 (2011).
2. Y. Yuan, Y.-H. E. Loh, X. Han, J. Feng, T.-V. Ho, J. He, J. Jing, K. Groff, A. Wu, Y. Chai, Spatiotemporal cellular movement and fate decisions during first pharyngeal arch morphogenesis. *Sci. Adv.* **6**, eabb0119 (2020).
3. W. Dai, X. Guo, Y. Cao, J. A. Mondo, J. P. Campanale, B. J. Montell, H. Burrous, S. Streichan, N. Gov, W.-J. Rappel, D. J. Montell, Tissue topography steers migrating *Drosophila* border cells. *Science* **370**, 987–990 (2020).
4. G. Li, T. Zheng, L. Wu, Q. Han, Y. Lei, L. Xue, L. Zhang, X. Gu, Y. Yang, Bionic microenvironment-inspired synergistic effect of anisotropic micro-nanocomposite topology and biology cues on peripheral nerve regeneration. *Sci. Adv.* **7**, eabi5812 (2021).
5. K. Duval, H. Grover, L.-H. Han, Y. Mou, A. F. Pegoraro, J. Fredberg, Z. Chen, Modeling physiological events in 2D vs. 3D cell culture. *Phys. Ther.* **32**, 266–277 (2017).
6. M. A. Lancaster, N. S. Corsini, S. Wolfinger, E. H. Gustafson, A. W. Phillips, T. R. Burkard, T. Otani, F. J. Livesey, J. A. Knoblich, Guided self-organization and cortical plate formation in human brain organoids. *Nat. Biotechnol.* **35**, 659–666 (2017).
7. C.-H. Yang, A. D. Antonio, G. W. Kirschen, P. Varma, J. Hsieh, S. Ge, Circuit integration initiation of new hippocampal neurons in the adult brain. *Cell Rep.* **30**, 959–968.e3 (2020).
8. V. N.-Estévez, J. Hsieh, Human brain organoid models of developmental epilepsies. *Epilepsy Curr.* **20**, 282–290 (2020).
9. I. R. Suhito, N. Angeline, K.-H. Lee, H. Kim, C. G. Park, Z. Luo, T.-H. Kim, A spheroid-forming hybrid gold nanostructure platform that electrochemically detects anticancer effects of curcumin in a multicellular brain cancer model. *Small* **17**, 2002436 (2021).
10. Z. R. Lybrand, S. Goswami, J. Zhu, V. Jarzabek, N. Merlock, M. Aktar, C. Smith, L. Zhang, P. Varma, K.-O. Cho, S. Ge, J. Hsieh, A critical period of neuronal activity results in aberrant neurogenesis rewiring hippocampal circuitry in a mouse model of epilepsy. *Nat. Commun.* **12**, 1423 (2021).
11. V. Nieto-Estevez, J. Hsieh, CHD2: One gene, many roles. *Neuron* **100**, 1014–1016 (2018).
12. Y. Zheng, X. Xue, A. M. Resto-Irizarry, Z. Li, Y. Shao, Y. Zheng, G. Zhao, J. Fu, Dorsal-ventral patterned neural cyst from human pluripotent stem cells in a neurogenic niche. *Sci. Adv.* **5**, eaax5933 (2019).
13. M. H.-Thorsager, J. G.-Mazariegos, S. T. Arold, E. K. Nadendla, P. Y. Bertucci, P. Germain, P. Tomançak, K. Pierzchalski, J. W. Jones, R. Albalat, M. A. Kane, W. Bourguet, V. Laudet, D. Arendt, M. Schubert, The ancestral retinoic acid receptor was a low-affinity sensor triggering neuronal differentiation. *Sci. Adv.* **4**, eaao1261 (2018).
14. M. Khazaei, C. S. Ahuja, H. Nakashima, N. Nagoshi, L. Li, J. Wang, J. Chio, A. Badner, D. Seligman, A. Ichise, S. Shibata, M. G. Fehlings, GDNF rescues the fate of neural progenitor grafts by attenuating Notch signals in the injured spinal cord in rodents. *Sci. Trans. Med.* **12**, eaau3538 (2020).
15. E. M. Ozbudak, M. Thattai, I. Kurtser, A. D. Grossman, A. van Oudenaarden, Regulation of noise in the expression of a single gene. *Nat. Genet.* **31**, 69–73 (2002).
16. D. Strebinger, C. Deluz, E. T. Friman, S. Govindan, A. B. Alber, D. M. Suter, Endogenous fluctuations of OCT4 and SOX2 bias pluripotent cell fate decisions. *Mol. Syst. Biol.* **15**, e9002 (2019).
17. T. Kimoto, R. Hosokawa, T. Kubo, M. Maeda, A. Sano, Y. Akagawa, Continuous administration of basic fibroblast growth factor (FGF-2) accelerates bone induction on rat calvaria—An application of a new drug delivery system. *J. Dent. Res.* **77**, 1965–1969 (1998).
18. Y. Suematsu, Y. A. Tsai, S. Takeoka, C. M. Franz, S. Araib, T. Fujie, Ultra-thin, transparent, porous substrates as 3D culture scaffolds for engineering ASC spheroids for high-magnification imaging. *J. Mater. Chem. B* **8**, 6999–7008 (2020).
19. H.-C. Zhou, J. R. Long, O. M. Yaghi, Introduction to metal–organic frameworks. *Chem. Rev.* **112**, 673–674 (2012).
20. L. E. Kreno, K. Leong, O. K. Farha, M. Allendorf, R. P. Van Duyne, J. T. Hupp, Metal–organic framework materials as chemical sensors. *Chem. Rev.* **112**, 1105–1125 (2012).
21. C. Wu, S. Zeng, Z. Wang, F. Wang, H. Zhou, J. Zhang, Z. Ci, L. Sun, Efficient mechanoluminescent elastomers for dual-responsive anticounterfeiting device and stretching/strain sensor with multimode sensibility. *Adv. Funct. Mater.* **28**, 1803168 (2018).
22. H. Deng, S. Grunder, K. E. Cordova, C. Valente, H. Furukawa, M. Hmadeh, F. Gándara, A. C. Whalley, Z. Liu, S. Asahina, H. Kazumori, M. O'Keeffe, O. Terasaki, J. F. Stoddart, O. M. Yaghi, Large-pore apertures in a series of metal-organic frameworks. *Science* **336**, 1018–1023 (2012).
23. U. Mueller, M. Schubert, F. Teich, H. Puetter, K. Schierle-Arndta, J. Pastréa, Metal–organic frameworks—Prospective industrial applications. *J. Mater. Chem.* **16**, 626–636 (2006).
24. C. C.-Blas, C. Á.-Galván, I. P.-Orench, A. G.-Sánchez, F. E. Oropeza, E. G.-Puebla, Á. Monge, V. A. de la P.-O'Shea, F. Gándara, Highly efficient multi-metal catalysts for carbon dioxide reduction prepared from atomically sequenced metal organic frameworks. *Nano Res.* **14**, 493–500 (2021).
25. T. Skorjanc, D. Shetty, F. Gándara, L. Ali, J. Raya, G. Das, M. A. Olson, A. Trabolsi, Remarkably efficient removal of toxic bromate from drinking water with a porphyrin–viologen covalent organic framework. *Chem. Sci.* **11**, 845–850 (2020).
26. J. D. Rocca, D. Liu, W. Lin, Nanoscale metal–organic frameworks for biomedical imaging and drug delivery. *Acc. Chem. Res.* **44**, 957–968 (2011).
27. P. Horcajada, C. Serre, G. Maurin, N. A. Ramsahye, F. Balas, M. Vallet-Regí, M. Sebban, F. Taulelle, G. Férey, Flexible porous metal-organic frameworks for a controlled drug delivery. *J. Am. Chem. Soc.* **130**, 6774–6780 (2008).
28. F. Benyettou, N. Kaddour, T. Prakasam, G. Das, S. K. Sharma, S. A. Thomas, F. B.-Sari, J. Whelan, M. A. Alkhalifah, M. Khair, H. Traboulsi, R. Pasricha, R. Jagannathan, N. Mokhtari-Soulimane, F. Gándara, A. Trabolsi, In vivo oral insulin delivery via covalent organic frameworks. *Chem. Sci.* **12**, 6037–6047 (2021).
29. Y. Li, C. Yang, F. Zheng, X. Ou, Q. Pan, Y. Liuab, G. Wang, High pyridine N-doped porous carbon derived from metal–organic frameworks for boosting potassium-ion storage. *J. Mater. Chem. A* **6**, 17959–17966 (2018).
30. T.-T. Chen, J.-T. Yi, Y.-Y. Zhao, X. Chu, Biomineralized metal–organic framework nanoparticles enable intracellular delivery and endo-lysosomal release of native active proteins. *J. Am. Chem. Soc.* **140**, 9912–9920 (2018).
31. Y. Chen, P. Li, J. A. Modica, R. J. Drout, O. K. Farha, Acid-resistant mesoporous metal–organic framework toward oral insulin delivery: Protein encapsulation, protection, and release. *J. Am. Chem. Soc.* **140**, 5678–5681 (2018).
32. S. R. Miller, D. Heurtaux, T. Baati, P. Horcajada, J.-M. Grenèche, C. Serre, Biodegradable therapeutic MOFs for the delivery of bioactive molecules. *Chem. Commun.* **46**, 4526–4528 (2010).
33. S. Zeng, Y. Liu, S. Li, K. Shen, Z. Hou, A. P. Chooi, A. T. Smith, Z. Chen, L. Sun, Smart laser-writable micropatterns with multiscale photo/moisture reconstructible structure. *Adv. Funct. Mater.* **31**, 2009481 (2021).
34. S. Zeng, K. Shen, S. Li, R. Li, Z. Hou, X. Zhang, W. R. T. Tait, T. Kajiwara, A. Takahara, A. T. Smith, M. D. Jones, D. Zhang, L. Sun, Tailoring multistimuli responsive micropatterns activated by various mechanical modes. *Adv. Funct. Mater.* **31**, 2100612 (2021).
35. C. Xuan, L. Hao, X. Liu, Y. Zhu, H. Yang, Y. Ren, L. Wang, T. Fujie, H. Wu, Y. Chen, X. Shi, C. Mao, Wet-adhesive, haemostatic and antimicrobial bilayered composite nanosheets for sealing and healing soft-tissue bleeding wounds. *Biomaterials* **252**, 120018 (2020).
36. A. Hasebe, Y. Suematsu, S. Takeoka, T. Mazzocchi, L. Vannozzi, L. Ricotti, T. Fujie, Biohybrid actuators based on skeletal muscle-powered microgrooved ultrathin films consisting of poly(styrene-block-butadiene-block-styrene). *ACS Biomater. Sci. Eng.* **5**, 5734–5743 (2019).
37. Y.-W. Cho, D.-S. Kim, I. R. Suhito, D. K. Han, T. Lee, T.-H. Kim, Enhancing neurogenesis of neural stem cells using homogeneous nanohole pattern-modified conductive platform. *Int. J. Mol. Sci.* **21**, 191 (2020).
38. J. H. Cavka, S. Jakobsen, U. Olsbye, N. Guillou, C. Lamberti, S. Bordiga, K. P. Lillerud, A new zirconium inorganic building brick forming metal organic frameworks with exceptional stability. *J. Am. Chem. Soc.* **130**, 13850–13851 (2008).
39. M. N. Marchetti, E. Sampol, H. Bun, H. Scoma, B. Lacarelle, A. Durand, In vitro metabolism of three major isomers of retinoic acid in rats: Intersex and interstrain comparison. *Drug Metab. Dispos.* **25**, 637–646 (1997).
40. J. R. Muindi, M. D. Roth, R. A. Wise, J. E. Connett, G. T. O'Connor, J. W. Ramsdell, N. W. Schluger, M. Romkes, R. A. Branch, F. C. Sciurba, Pharmacokinetics and metabolism of all-trans-and 13-cis-retinoic acid in pulmonary emphysema patients. *J. Clin. Pharmacol.* **48**, 96–107 (2008).
41. L. Panzella, P. Manini, A. Napolitano, M. d'Ischia, Free radical oxidation of (E)-retinoic acid by the Fenton reagent: Competing epoxidation and oxidative breakdown pathways and novel products of 5,6-epoxyretinoic acid transformation. *Chem. Res. Toxicol.* **17**, 1716–1724 (2004).
42. M. A. Kane, N. Chen, S. Sparks, J. L. Napoli, Quantification of endogenous retinoic acid in limited biological samples by LC/MS/MS. *Biochem. J.* **388**, 363–369 (2005).

ScienceAdvances

Single metal-organic framework–embedded nanopit arrays: A new way to control neural stem cell differentiation

Yeon-Woo ChoSeohyeon JeeIntan Rosalina SuhitoJeong-Hyeon LeeChun Gwon ParkKyung Min ChoiTae-Hyung Kim

View the article online
https://www.science.org/doi/10.1126/sciadv.abj7736
Permissions
https://www.science.org/help/reprints-and-permissions

Use of this article is subject to the Terms of service